Implications of first neutrino-induced nuclear recoil measurements in direct detection experiments

D. Aristizabal Sierra,[1, *] N. Mishra,[2, †] and L. Strigari[2, ‡]

[1]*Universidad Técnica Federico Santa María - Departamento de Física*
Casilla 110-V, Avda. España 1680, Valparaíso, Chile
[2]*Department of Physics and Astronomy, Mitchell Institute for Fundamental Physics and Astronomy,*
Texas A&M University, College Station, Texas 77843, USA

PandaX-4T and XENONnT have recently reported the first measurement of nuclear recoils induced by the ^{8}B solar neutrino flux, through the coherent elastic neutrino-nucleus scattering (CEvNS) channel. As long anticipated, this is an important milestone for dark matter searches as well as for neutrino physics. This measurement means that these detectors have reached exposures such that searches for low mass, $\lesssim 10$ GeV dark matter cannot be analyzed using the background-free paradigm going forward. It also opens a new era for these detectors to be used as neutrino observatories. In this paper we assess the sensitivity of these new measurements to new physics in the neutrino sector. We focus on neutrino non-standard interactions (NSI) and show that—despite the still moderately low statistical significance of the signals—these data already provide valuable information. We find that limits on NSI from PandaX-4T and XENONnT measurements are comparable to those derived using combined COHERENT CsI and LAr data, as well as those including the latest Ge measurement. Furthermore, they provide sensitivity to pure τ flavor parameters that are not accessible using stopped-pion or reactor sources. With further improvements of statistical uncertainties as well as larger exposures, forthcoming data from these experiments will provide important, novel results for CEvNS-related physics.

I. INTRODUCTION

PandaX-4T [1] and XENONnT [2] have recently reported the detection of coherent elastic neutrino-nucleus scattering (CEvNS) induced by ^{8}B solar neutrinos. Due to their low energy thresholds and large active volumes these experiments identify the ^{8}B component of the solar neutrino flux at a significance level of the order of 2σ. This is the first detection of CEvNS from an astrophysical source, complementing the recent detections from the stopped-pion source by the COHERENT experiment [3–5]. Further, this detection probes the CEvNS cross section at characteristic neutrino energy scales lower than that probed by COHERENT and with a new material target[1].

The detection of solar neutrinos at dark matter (DM) detectors such as PandaX-4T and XENONnT is a milestone in neutrino physics [6–10]. It represents an important step in the continuing development of the solar neutrino program, dating back to over half of a century. From the perspective of solar neutrino physics, it is the second pure neutral current channel detection of the solar neutrino flux, complementing the SNO neutral current detection of the flux using a deuterium target [11]. Its observation was anticipated long time ago to be not only a challenge for DM searches, but also an opportunity for a better understanding of neutrino properties and searches of new physics [12].

The detection of ^{8}B neutrinos via CEvNS has important implications more broadly for neutrino physics, astrophysics, and DM. This detection has the potential to provide information on the properties of the solar interior [13]. It also

has the potential to probe new physics in the form of non-standard neutrino interactions (NSI) [14–17], sterile neutrinos [18, 19], neutrino electromagnetic properties [20–23] or new interactions involving light mediators [16, 24]. Detection of solar neutrinos via CEvNS also is important for interpreting the possible detection of low mass, $\lesssim 10$ GeV, dark matter [25, 26]. A detailed understanding of this signal is of paramount importance for the interpretation of future data. The identification of a possible WIMP signal requires a thorough understanding of neutrino-induced nuclear recoils.

In this paper, we examine the sensitivity of the PandaX-4T and XENONnT data to NSI. We show that even with this early data these measurements are already capable of providing competitive bounds. In particular, because of neutrino flavor conversion, these measurements are sensitive to all neutrino flavors and so open flavor channels not accessible in CEvNS experiments relying on π^+ decay-at-rest or reactor neutrino fluxes. Thus from this point of view these experiments are very unique.

The reminder of this paper is organized as follows. In Sec. II we discuss the Standard Model (SM) CEvNS cross section, define the parameters we use in our calculation and briefly discuss the experimental input employed. In Sec. II we provide a detailed discussion of NSI effects in both propagation and detection. To do so we rely on the two-flavor approximation, which provides rather reliable results up to corrections of $\sim 10\%$ [2]. In Sec. IV, after briefly discussing the main features of both PandaX-4T and XENONnT data, we present the results of our analysis. Finally, in Sec. V we summarize and present our conclusions. In App. A we provide a summary of NSI limits arising from the one-parameter analysis.

---

* daristizabal@uliege.be
† nityasa˙mishra@tamu.edu
‡ strigari@tamu.edu
[1] Measurements at COHERENT have employed CsI, LAr and more recently Ge. Both PandaX-4T and XENONnT, instead, rely on LXe.

---

[2] Note that both PandaX-4T and XENONnT data have statistical uncertainties of the order of 37% [1, 2]. Theoretical precision below 10% is therefore at this stage not required.

Flux	Normalization [$\text{cm}^{-2}\text{s}^{-1}$]	End-point [MeV]
pp	5.98×10^{10}	0.40
^7Be	4.93×10^{9}	$0.38, 0.86$
pep	1.44×10^{8}	1.44
^{13}N	2.78×10^{8}	1.20
^{15}O	2.05×10^{8}	1.73
^{17}F	5.29×10^{6}	1.74
^8B	5.46×10^{6}	16.0
hep	7.98×10^{3}	18.7

TABLE I. Neutrino flux normalization as recommended in Ref. [35] and inline with the B16(GS98) SSM. For detection only ^{8}B matters. For propagation we include the whole spectrum.

II. CEvNS CROSS SECTION, ^{8}B SOLAR NEUTRINO FLUX, EVENT RATES AND EXPERIMENTAL INPUT

In the SM, at tree-level the CEvNS cross section is has no lepton flavor dependence [27], with flavor-dependent corrections appearing at the one-loop level [28–30]. At tree level the scattering cross section reads [27]

$$\frac{d\sigma}{dE_r} = \frac{G_F^2}{2\pi} Q_W^2 \, m_N \left(2 - \frac{m_N E_r}{E_\nu^2}\right) F_W^2(E_r) \, . \quad (1)$$

For the nuclear mass, m_N, we use the averaged mass number $\langle A \rangle = \sum_{i=1}^{9} X_i A_i$, where i runs over the nine stable xenon isotopes and X_i refers to i-th isotope natural abundance. Q_W refers to the weak charge and determines the strength at which the Z gauge boson couples to the nucleus. At tree-level and neglecting q^2 dependent terms (q referring to the transferred momentum) the weak charge is entirely determined by the vector neutron and proton couplings

$$Q_W = Z g_V^p + N g_V^n \, , \quad (2)$$

with $Z = 54$ referring to the nucleus atomic number and $N = (\langle A \rangle - Z)$ to the number of neutrons. The nucleon couplings are in turn given by the fundamental electroweak neutral current up and down couplings: $g_V^p = 1/2 - 2\sin^2\theta_W$ and $g_V^n = -1/2$. Because of the value of the weak mixing angle[3], g_V^n exceeds g_V^p by more than a factor 20. Thus, up to small corrections the total cross section scales as $N^2 = (A - Z)^2$.

Effects due to the finite size of the nucleus are parameterized in terms of the weak-charge form factor, F_W, for which different parametrizations can be adopted. However, given the energy scale of solar neutrinos these finite size nuclear effects are small, not exceeding more than a few percent regardless of the parametrization [32, 33]. Although of little

impact, our calculation does include the weak-charge form factor. We have adopted the Helm parametrization [34] along with $R_n = R_C + 0.2\,\text{fm}$, with R_C calculated by averaging the charge radius of each of the nine xenon stables isotopes over their natural abundance.

^{8}B electron neutrinos are produced in β^+ decay processes: $^8\text{B} \rightarrow \text{Be}^* + e^+ + \nu_e$. The features of the spectrum as well as its normalization is dictated by the Standard Solar Model (SSM). In our analysis we use the values predicted by the B16(GS98) SSM [36]. The distribution of ^{8}B neutrino production from the B16(GS98) SSM peaks at around $5 \times 10^{-2} R_\odot$ and ceases to be efficient at $0.1 R_\odot$, where the distribution fades away. For the calculation of event rates only the ^{8}B neutrino flux is required. For the calculation of propagation effects (matter effects), however, we require all possible fluxes. In all cases we adopt neutrino spectra normalization as recommended for reporting results for direct DM searches [35], which are inline with those predicted by the B16(GS98) SSM. The values for those normalization factors along with the kinematic end-point energies for all fluxes are shown in Tab. I.

Calculation of differential event rate spectra follows from convoluting the CEvNS differential cross section in Eq. (1) with the ^{8}B spectral function, namely

$$\frac{dR}{dE_r} = \frac{\varepsilon N_A}{m_{\text{mol}}^{\text{Xe}}} N_{^8\text{B}} \int_{E_\nu^{\min}}^{E_\nu^{\max}} \frac{d\Phi_{^8\text{B}}}{dE_\nu} \frac{d\sigma}{dE_r} dE_\nu \, . \quad (3)$$

Here ε refers to exposure measured in tonne-year, N_A is the Avogadro number in 1/mol units, $m_{\text{mol}}^{\text{Xe}} = 131.3 \times 10^{-3}\text{kg/mol}$, $N_{^8\text{B}}$ the ^{8}B flux normalization from Tab. I, $E_\nu^{\min} = \sqrt{m_N E_\nu/2}$ and $E_\nu^{\max}$ the kinematic end-point of the ^{8}B spectrum from Tab. I as well. Eq. (3) is valid in the SM, where the CEvNS differential cross section is flavor universal at tree level. If either through one-loop corrections or new physics the cross section becomes flavor dependent, then the integrand should involve the probability associated with each neutrino flavor (see Sec. III B for a more detailed discussion). The event rate follows from integration of Eq. (3) over recoil energies, with the experimental acceptance $\mathcal{A}(E_r)$ fixed according to the PandaX-4T or XENONnT data sets. Generically it reads

$$R = \int_{E_r^{\min}}^{E_r^{\max}} \mathcal{A}(E_r) \frac{dR}{dE_r} dE_r \, . \quad (4)$$

PandaX-4T perform two types of analyses on their data. First, they perform a combined S1/S2 analysis, in which a neutrino signal event is identified via both prompt scintillation and secondary ionization signals from the nuclear recoil (*paired signal*). The low energy threshold for this analysis is set by the S1 signal, which in terms of nuclear recoil energy is ~ 1.1 keV. The second analysis is an S2 only analysis, in which only the ionization component is used as the signal of an event (*US2 signal*). In this case, the nuclear recoil threshold is lower, ~ 0.3 keV, but the trade-off is an increase in the backgrounds for this sample.

PandaX-4T present data from two runs: their commissioning run, which they call Run0, and their first science run, which they call Run1. For the paired data set, the exposure is

---
[3] In our analysis we use the SM central value prediction extrapolated to low energies ($q = 0$), $\sin^2\theta_W = 0.23857 \pm 0.00003$ [31].

Data set	Exp [tonne-year]	$E_r^{\mathrm{min,max}}$ [keV]	Signal
PandaX-4T (paired)	1.25	1.1/3.0	3.5 ± 1.3
PandaX-4T (US2)	1.04	0.3/3.0	75 ± 28
XENONnT	3.51	0.5/3.0	10.7 ± 3.95

TABLE II. PandaX-4T (paired and US2) and XENONnT parameter detector configurations used in the NSI statistical analysis. Values taken from Refs. [1, 2].

1.25 tonne-year, and for the US2, the exposure is 1.04 tonne-year. Using a maximum likelihood analysis, PandaX-4T finds a best fitting ^{8}B event rate from the US2 sample of 75 ± 28 and a paired event rate of 3.5 ± 1.3.

The XENONnT collaboration combined two separate analyses, labelled SR0 and SR1, which when combined amount to an exposure of 3.51 tonne-year. They present acceptances for both an S1 only and an S2 only analysis. For the primary analysis, XENONnT combine the acceptances for S1 and S2 (with a resulting 0.5 keV threshold), and, for this combined exposure, they quote a best fit event rate of $10.7^{+3.7}_{-4.2}$. They point out that this result is in close agreement with: (i) Expectations from the measured solar ^{8}B neutrino flux from SNO, (ii) the theoretical CEvNS cross section with xenon nuclei, (iii) calibrated detector response to low-energy nuclear recoils. For the expected event rate, they find $11.9^{+4.5}_{-4.2}$. Calculation of the Z-score—assuming these results to be independent—yields 0.2σ. Thus using either in our statistical procedure produces no sizable deviation in the final results. Tab. II summarizes the detector parameter configurations along with the signals we have employed.

III. NEUTRINO NON-STANDARD INTERACTIONS

In addition to loop-level corrections, flavor-dependence in the CEvNS cross section may also be introduced through neutrino NSI [37]. The effective Lagrangian accounting for the new vector interactions can be written as

$$\mathcal{L}_{\mathrm{NSI}} = -\sqrt{2} G_F \sum_{\substack{i=e,\mu,\tau \\ q=u,d}} \bar{\nu}_i \gamma_\mu P_L \varepsilon_{ij}^q \nu_j \bar{q} \gamma^\mu q \,, \qquad (5)$$

where the ε_{ij}^q parameters determine the strength of the effective interaction with respect to the SM strength. Neutrino NSI affect neutrino production, propagation and detection. Since production takes place through charged-current (CC) processes, effects in production are small [4]. Effects on propagation and detection, being due to neutral current, can instead be potentially large. Thus we consider only those two. Propagation effects arise from forward scattering processes which

———————

[4] For instance, off-diagonal CC NSI can induce charged lepton rare decays for which stringent bounds apply. Diagonal CC NSI can induce contact $e^- e^+ q\bar{q}$ interactions for which collider limits apply too.

induce matter potentials proportional to the number density of the scatterers. So in addition to the SM matter potential, the new interaction—being of vector type—induces additional matter potentials that affect neutrino propagation and thus neutrino flavor conversion. Detection, instead, becomes affected because of the impact of the new effective interaction on the CEvNS cross section. All in all, NSI effects on solar neutrinos may be prominent in propagation $\oplus$ detection.

Neutrino NSI are constrained by a variety of experimental searches. Here we provide a summary of the main constraints, which does not aim at being complete but rather to provide a general picture of what has been done (for a more detailed account see e.g. Ref. [38]). First of all, global analysis of oscillation data imply tight constraints on the size and flavor structure of matter effects. Thus, those constraints can be translated into limits on NSI parameters [39, 40]. Limits involving global analysis of oscillation data combined with CEvNS measurements have been also derived [41, 42]. Constraints from CEvNS data alone, for which only effects on detection apply, have been analyzed using both CsI data releases along with LAr data in Ref. [43], and also the most recent measurement with germanium in Ref. [44]. Further constraints from monojets and missing energy searches at the LHC exist [45, 46]. Involving electrons and at early times, the new interaction can keep neutrinos in thermal contact with electrons and positrons below $\sim 1\,\mathrm{MeV}$. Requiring small departures from this value leads to cosmological constraints [47]. In supernovæ, neutrino NSI have as well been considered in e.g. Refs. [48, 49].

In what follows we describe their effects in propagation and in detection. To do so we rely on the two-flavor approximation, well justified up to corrections of the order of 10% because of $\Delta m_{12}^2 / \Delta m_{13}^2 \ll 1$ and $\sin^2 \theta_{13} \ll 1$ [50]. And rather than including the data and constraints discussed above, we focus only on the constraints implied by PandaX-4T and XENONnT.

A. Neutrino NSI: Propagation effects

Electron neutrinos are subject to flavor conversion in the Sun, governed by the vacuum and matter Hamiltonians

$$i \frac{d}{dr} |\nu\rangle = \left[\frac{1}{2E_\nu} U H_{\mathrm{vac}} U^\dagger + H_{\mathrm{mat}} \right] |\nu\rangle \,. \qquad (6)$$

Here $|\nu\rangle^T = |\nu_e, \nu_\mu, \nu_\tau\rangle^T$ refers to the neutrino flavor eigenstate basis, r to the neutrino propagation path, $U = U_{23} U_{13} U_{12} \equiv U(\theta_{23}) U(\theta_{13}) U(\theta_{12})$ is the 3×3 leptonic mixing matrix parametrized in the standard way, $H_{\mathrm{vac}} = \mathrm{diag}(0, \Delta m_{21}^2, \Delta m_{31}^2)$ and in the absence of NSI the matter Hamiltonian is given by $H_{\mathrm{mat}} = \sqrt{2} G_F n_e(r) \mathrm{diag}(1,0,0)$. Note that because of matter potentials neutrino flavor evolution is more conveniently followed in the flavor basis.

As previously pointed out, the presence of neutrino NSI induce new matter potential terms that modify the flavor evolu-

tion equation, namely

$$i\frac{d}{dr}|\nu\rangle = \left[\frac{1}{2E_\nu}U\,H_{\text{vac}}\,U^\dagger + \sqrt{2}G_F n_e(r)\sum_{f=e,u,d}\varepsilon^f\right]|\nu\rangle \ , \quad (7)$$

where the NSI coupling matrices ε^f involves the quark relative abundances in addition to the parameters entering in Eq. (17):

$$\varepsilon^f = \begin{pmatrix} 1+\varepsilon^f_{ee} & \varepsilon^f_{e\mu} & \varepsilon^f_{e\tau} \\ \varepsilon^f_{e\mu} & \varepsilon^f_{\mu\mu} & \varepsilon^f_{\mu\tau} \\ \varepsilon^f_{e\tau} & \varepsilon^f_{\mu\tau} & \varepsilon^f_{\tau\tau} \end{pmatrix} \ . \quad (8)$$

Explicitly, $\varepsilon^f_{ij}(r) = Y_f(r)\varepsilon^f_{ij}$ $(f = e, u, d)$ with $Y_f(r) = n_f(r)/n_e(r)$. The up- and down-quark relative abundances are written in terms of the neutron relative abundance $Y_u = 2+Y_n$ and $Y_d = 1+2Y_n$, with the neutron number density calculated from the ^{4}He and ^{1}H mass fractions.

A three-flavor analysis of NSI matter effects demands numerical integration of Eq. (7) for each point in the NSI parameter space. However, an analytical, less CPU expensive and yet precise approach can be adopted in the so-called mass dominance limit $\Delta m^2_{13} \to \infty$ [40]. In this approximation, neutrino propagation is properly described in the basis $|\widetilde{\nu}\rangle = \mathcal{U}^T|\nu\rangle \equiv U^T_{13}U^T_{23}|\nu\rangle$ (*propagation basis*). Up to corrections of the order of $\sin\theta_{13}$, the propagating neutrino states are: A mainly electron neutrino state ($\tilde{\nu}_e$), a superposition of muon and tau neutrinos state ($\tilde{\nu}_\mu$) and its orthogonal counterpart ($\tilde{\nu}_\tau$). With these considerations, only $\tilde{\nu}_e$ and $\tilde{\nu}_\mu$ have sizable mixing. Mixing with $\tilde{\nu}_\tau$ for neutrino energies of the order of 10 MeV and average SSM quark number densities does not exceed $3\times 10^{-2}\times\varepsilon^q_{ij}$ [15]. With $\tilde{\nu}_\tau$ "decoupled" from mixing, flavor conversion becomes then a two-flavor problem that can be entirely treated at the analytic level.

In two-flavor approximation, the survival probability is given by $\mathcal{P}_{ee}(E_\nu,r)$ [40]

$$\mathcal{P}_{ee}(E_\nu,r) = \cos^4\theta_{13}\,\mathcal{P}_{\text{eff}}(E_\nu,r) + \sin^4\theta_{13} \ , \quad (9)$$

where the r dependence is introduced by the effective probability given by [51]

$$\mathcal{P}_{\text{eff}}(E_\nu,r) = \frac{1+\cos 2\theta_M(r)\cos 2\theta_{12}}{2} \ . \quad (10)$$

Here $\theta_M(r)$ is the mixing angle in matter and adiabatic propagation has been assumed, thus implying a rather suppressed level-crossing probability ($P_c \to 0$). With neutrino oscillation data taken from Ref. [50], calculation of the survival probability in Eq. (9) then reduces to the determination of θ_M. To do so the following 2×2 Hamiltonian has to be diagonalized

$$H = \frac{1}{4E_\nu}\begin{pmatrix} -\Delta m^2_{21}\cos 2\theta_{12}+A & \Delta m^2_{21}\sin 2\theta_{12}+B \\ \Delta m^2_{21}\sin 2\theta_{12}+B & \Delta m^2_{21}\cos 2\theta_{12}-A \end{pmatrix} \ . \quad (11)$$

In this expression the A and B terms in the diagonal and off-diagonal entries are given by

$$A = 4\sqrt{2}E_\nu G_F n_e(r)\left[\frac{\cos^2\theta_{13}}{2}-Y_q(r)\varepsilon^q_D\right] \ ,$$
$$B = 4\sqrt{2}E_\nu G_F n_e(r)Y_q(r)\varepsilon^q_N \ , \quad (12)$$

from where it can be seen that in the limit $\varepsilon^q_{ij}=0$ and $\cos\theta_{13}=0$, A reduces to the SM term and B vanishes. The parameters ε_D and ε_N result from the rotation from the flavor to the propagation basis and read [40]:

$$\varepsilon^q_D = -\frac{c^2_{13}}{2}\varepsilon^q_{ee} + \frac{[c^2_{13}-(s^2_{23}-s^2_{13}c^2_{23})]}{2}\varepsilon^q_{\mu\mu} + \frac{(s^2_{23}-c^2_{23}s^2_{13})}{2}\varepsilon^q_{\tau\tau} + s_{13}c_{13}s_{23}\varepsilon^q_{e\mu} + s_{13}c_{13}c_{23}\varepsilon^q_{e\tau} - (1+s^2_{13})c_{23}s_{23}\varepsilon^q_{\mu\tau} \ , \quad (13)$$
$$\varepsilon^q_N = -s_{13}c_{23}s_{23}\varepsilon^q_{\mu\mu} + s_{13}c_{23}s_{23}\varepsilon^q_{\tau\tau} + c_{13}c_{23}\varepsilon^q_{e\mu} - c_{13}s_{23}\varepsilon^q_{e\tau} + s_{13}\left(s^2_{23}-c^2_{23}\right)\varepsilon^q_{\mu\tau} \ , \quad (14)$$

where $c_{ij} \equiv \cos\theta_{ij}$ and $s_{ij} \equiv \sin\theta_{ij}$. The mixing angle in matter thus can be written as

$$\cos 2\theta_M(r) = \frac{\Delta m^2_{12}\cos 2\theta_{12}-A}{\sqrt{\left(\Delta m^2_{12}\cos 2\theta_{12}-A\right)^2 + \left(\Delta m^2_{12}\sin 2\theta_{12}+B\right)^2}} \ . \quad (15)$$

Eqs. (9) and (10) combined with Eqs. (12)-(15) allow the determination of $\mathcal{P}_{ee}(E_\nu,r)$ in terms of neutrino oscillation parameters, electron and quark number densities and NSI parameters. The averaged survival probability is then obtained by integrating over r taking into account the distribution of

neutrino production in the Sun [40]:

$$\langle\mathcal{P}_{ee}(E_\nu)\rangle = \frac{\sum_\alpha\Phi_\alpha(E_\nu)\int_0^1 dr\rho(r)\,\mathcal{P}_{ee}(E_\nu,r)}{\sum_\alpha\Phi_\alpha(E_\nu)} \ , \quad (16)$$

where $\Phi_\alpha(E_\nu)$ refers to the α component of the solar neutrino flux (with α running over all components) and $\rho_\alpha(r)$ to the distribution of neutrino production. For illustration (and only with that aim), in Fig. 1 we show an example of the averaged survival probability as a function of the neutrino energy for the case in which all couplings but ε^u_{ee} vanish. As can be seen, the new interaction can either enhance or deplete neutrino flavor conversion depending on its strength and on whether it reinforces or weakens the SM matter potential. With propagation effects already discussed and summarized in Eq. (16) we now
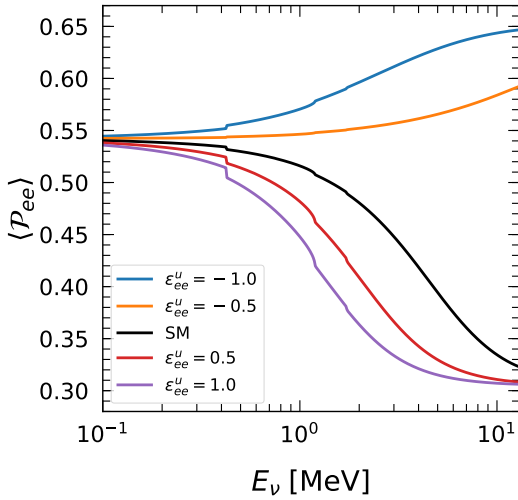
FIG. 1. Averaged survival probability as a function of neutrino energy for the case in which only ε_{ee}^u has a non-vanishing value. This graph aims only at illustrating the impact of neutrino NSI on neutrino propagation in the Sun. The different features are related with the kinematic end-points where certain neutrino fluxes fade away [see Tab. I along with Eq. (16)].

turn to the discussion of detection effects.

B. Neutrino NSI: Detection effects

For consistency, the same basis used for neutrino propagation should be used in neutrino detection as well. In doing so the effective Lagrangian in Eq. (17) reads

$$\mathcal{L}_{\text{NSI}} = -\sqrt{2} G_F \sum_{\substack{i=e,\mu,\tau \\ q=u,d}} \overline{\widetilde{\nu}}_i \gamma_\mu P_L \widetilde{\varepsilon}_{ij}^q \widetilde{\nu}_j \overline{q} \gamma^\mu q \,, \qquad (17)$$

where $\widetilde{\varepsilon}^q = \mathcal{U}^T \varepsilon^q \mathcal{U} \equiv U_{13}^T U_{23}^T \varepsilon^q U_{23} U_{13}$. With the couplings rotated this way the weak-charge in the CEvNS cross section in Eq. (1) becomes lepton flavor dependent, with the weak-charge in initial-state flavor i given by

$$Q_{\nu_i}^2 = \left[+N \left(g_V^n + \widetilde{\varepsilon}_{ii}^u + 2\widetilde{\varepsilon}_{ii}^d \right) + Z \left(g_V^p + 2\widetilde{\varepsilon}_{ii}^u + \widetilde{\varepsilon}_{ii}^d \right) \right]^2 + \sum_{j \neq i} \left[N \left(\widetilde{\varepsilon}_{ij}^u + 2\widetilde{\varepsilon}_{ij}^d \right) + Z \left(2\widetilde{\varepsilon}_{ij}^u + \widetilde{\varepsilon}_{ij}^d \right) \right]^2 \,. \qquad (18)$$

The couplings entering in the weak charge can be readily calculated from their definition, with the rotation matrices parametrized for a passive rotation: $\widetilde{\varepsilon}_{ij}^q = \sum_{k,\ell} \mathcal{U}_{ki} \varepsilon_{k\ell}^q \mathcal{U}_{\ell j}$. The effects of the NSI are then clear. By modifying the weak-charge the new interactions can either enhance of deplete the expected reaction rate. Eq. (18) shows that diagonal couplings can produce constructive or destructive interference, while off-diagonal couplings cannot. Note that a proper definition of the flavor basis is, in principle, not possible in the presence of flavor off-diagonal NSI parameters. Strictly speaking then a consistent treatment of such cases requires a density matrix formulation for the calculation of event rates [42]. Arguably, however, differences between the "standard" approach and the latter are expected to be small provided the off-diagonal parameters are suppressed. That this is the case is somehow expected from data, which do not sizably deviates from the SM expectation. Thus, we adopt the standard procedure regardless of the flavor structure of the parameters considered.

In the two-flavor approximation, two neutrino flavors reach the detector: $\widetilde{\nu}_e$ and $\widetilde{\nu}_\mu$. Lepton flavor composition of the final state, however, depends on the lepton flavor structure of the interaction. In full generality, the differential event rate is then written as follows

$$\frac{dR}{dE_r} = \sum_{k=e,\mu,\tau} \left(\frac{dR_{ek}}{dE_r} + \frac{dR_{\mu k}}{dE_r} \right) \,. \qquad (19)$$

Here the flavored differential event rates are obtained from

Eq. (3) by trading $Q_W \to Q_{\nu_i}$ and by taking into account the survival probability, $\langle \mathcal{P}_{ee} \rangle$, in the first term as well as the oscillation probability to the $\widetilde{\nu}_\mu$ state, $1 - \langle \mathcal{P}_{ee} \rangle$, in the second term. Thus, in the first (second) differential event rate in Eq. (19) couplings $\widetilde{\varepsilon}_{ek}^q$ $(\widetilde{\varepsilon}_{\mu k}^q)$ contribute. These couplings are a superposition of the NSI parameters we started with, so in a single-parameter analysis (which we adopt in the first part in Sec. IV) a non-vanishing unrotated NSI parameter can imply the presence of multiple rotated parameters at the cross section level.

IV. ANALYSIS AND RESULTS

The general problem of assessing the impact of neutrino NSI parameters in neutrino-nucleus event rates involves twelve independent couplings. It is of course a very CPU expensive problem, but not only that. With only a few observables to rely upon, little can be said in the most general case. For practical reasons and as well to make contact with previous analysis, we adopt a single-parameter approach. Towards the end of this section we consider the three lepton flavor diagonal two-parameter cases $(\varepsilon_{ee}^u, \varepsilon_{ee}^d)$, $(\varepsilon_{\mu\mu}^u, \varepsilon_{\mu\mu}^d)$ and $(\varepsilon_{\tau\tau}^u, \varepsilon_{\tau\tau}^d)$; as well to make contact with what has been done previously in the literature (the e and μ cases motivated by previous COHERENT data analysis). It is worth mentioning that because of neutrino flavor mixing multi-ton DM detectors are sensitive
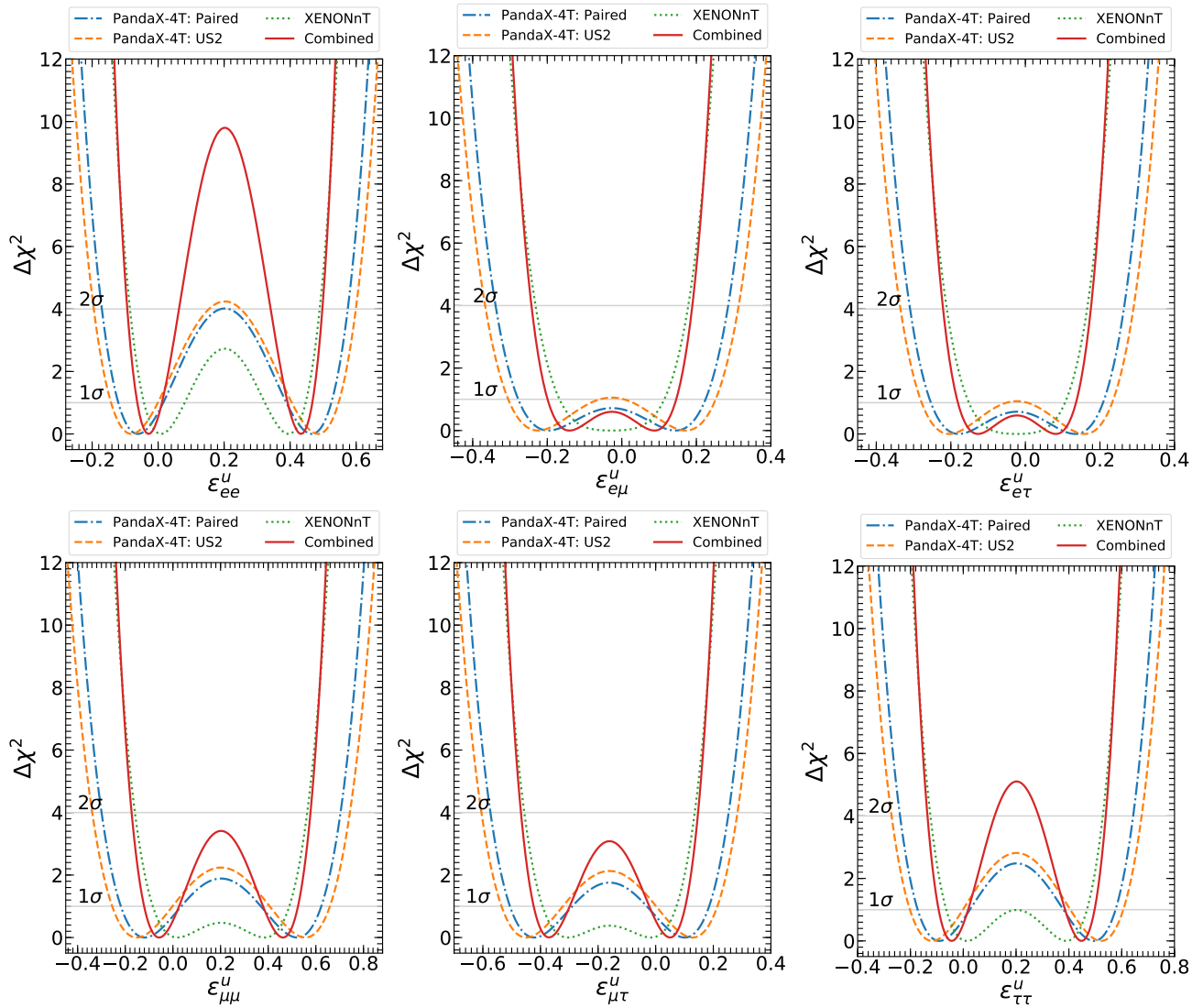
FIG. 2. Dependence of the $\Delta\chi^2$ function on the up-quark NSI parameters for the PandaX-4T [paired and unpaired ionization-only signals (US2)] as well as for XENONnT data sets. Results for the combined analysis are shown as well. The 1σ and 2σ confidence level values (horizontal lines) are shown to facilitate reading.

to τ flavor, which neither reactor nor stopped-pion sources are. From this point of view these measurements are unique.

We start with u-quark couplings and proceed by defining a simple χ-square test

$$\chi^2 = \left(\frac{R_{\text{Exp}} - R_{\text{SM+NSI}}}{\sigma_{\text{Exp}}} \right)^2 , \qquad (20)$$

where R_{Exp} refers to PandaX-4T and XENONnT event rates central values and (see Tab. II) and $R_{\text{SM+NSI}}$ to the SM events rates including as well NSI contributions. Though oversimplified, such χ-square statistic allows to capture the main features of the data sets and their sensitivity to NSI parameters. Results are shown in Fig. 2. First of all, in all cases and with all data sets two minima are found. This result follows from allowing the NSI parameter to have positive and negative values. Because of this range, as we have already pointed out,

event rates are symmetric around a small value. Experimental results are thus reproduced in two non-overlapping regions of parameter space.

One can see, however, the regions tend to be less pronounced for the XENONnT analysis, regardless of the NSI parameter. Statistical uncertainties are of the order of $\sim 37\%$ in all cases, so they cannot account for this behavior. We thus understand this tendency to be related with measured values and the SM expectation, as we now discuss. We find for the SM predicted values 2.4:46.8:11.3 events for paired:US2:XENONnT. Experimental ranges are on the other hand [2.2,4.8]:[47.0,103.0]:[6.7,14.6] for paired:US2:XENONnT. So, PandaX-4T results tend to prefer values above the SM prediction, while the SM value expected at XENONnT is well within the measured interval. In fact, the expected SM value is 5% away from the midrange, 10.65
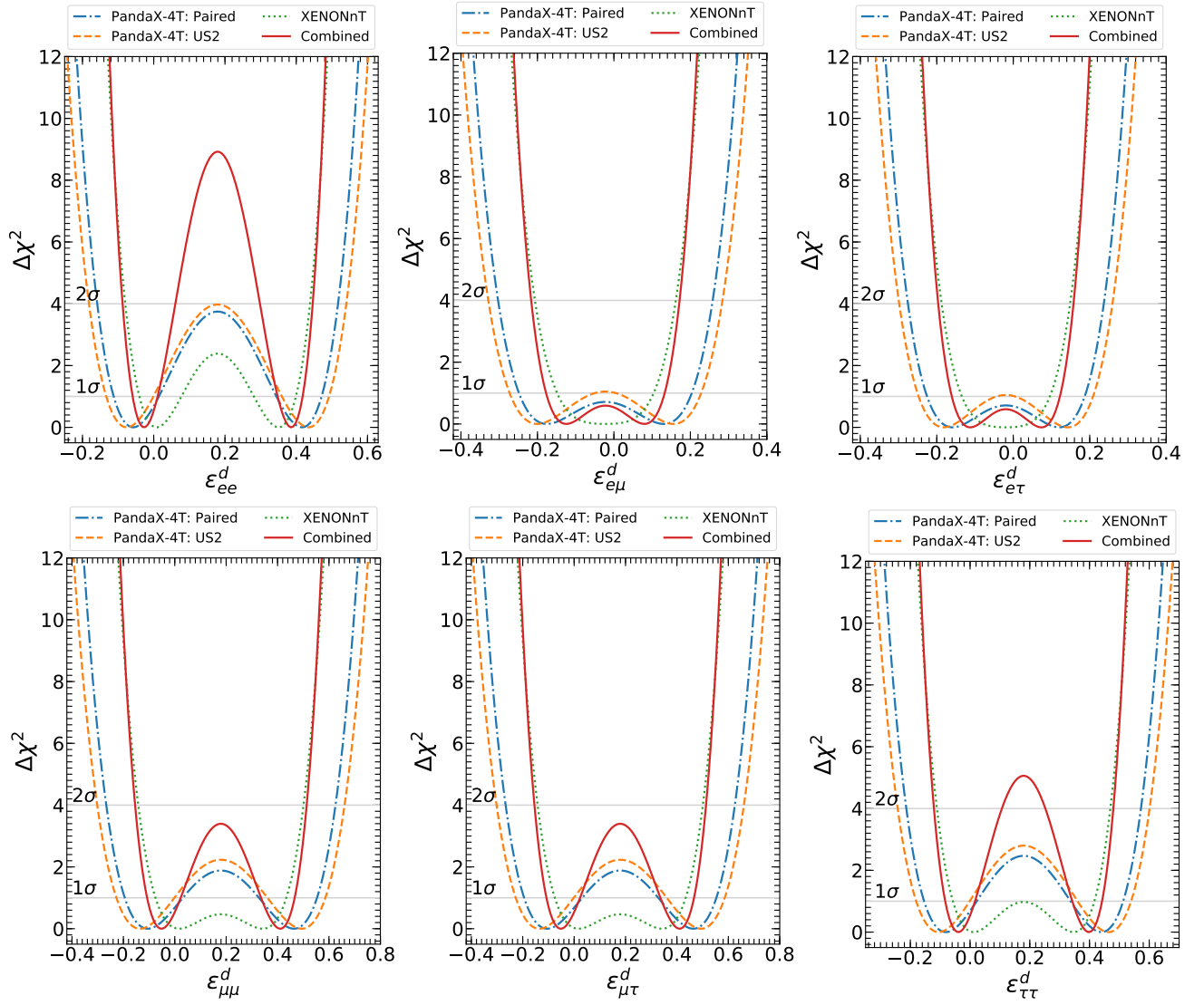
FIG. 3. Dependence of the $\Delta\chi^2$ function on the down-quark NSI parameters for the PandaX-4T [paired and unpaired ionization-only signals (US2)] as well as for XENONnT data sets. Results for the combined analysis are shown as well. The 1σ and 2σ confidence level values (horizontal lines) are shown to facilitate reading.

events.

From the results one can see that narrower 1σ level ranges are found for flavor-diagonal parameters. Results for flavor off-diagonal couplings are, instead, wider. This is as well expected. At the cross section level flavor-diagonal contributions add/subtract linearly to the SM contribution, while flavor off-diagonal do quadratically. Since $|\varepsilon_{ij}^{u}| < 1.0$, the diagonal components lead to larger deviations than the off-diagonal do for larger values.

We provide as well results from a combined analysis, that we have generated by constructing a combined chi-square test $\chi^2_{\text{Combined}} = \chi^2_{\text{Paired}} + \chi^2_{\text{US2}} + \chi^2_{\text{XENONnT}}$. These results, how-ever, should be interpreted with certain caution. Combining PandaX-4T and XENONnT this way is certainly reliable, but combining paired and US2 data sets might be not because of possible correlations. Very likely the most suitable way

of combining these data sets is through a covariance matrix. However, such an analysis can only be performed with the full data sets, including backgrounds. it can be noted that the combined analysis is dominated by XENONnT data, with the reason being what we pointed out already: XENONnT mea-surement is more inline with the SM expectation.

Results for down-quark couplings are shown in Fig. 3. Dif-ferences between these results and those found in the up-quark case are small, a result which is also expected. From a simple inspection of Eqs. (13) and (14) one can see that at the av-eraged survival probability level they enter in the same func-tional form. Differences between up and down quarks arise only through their relative abundance, for which in the region of interest (0.1 $R_{\odot}$) Y_u differs by no more than 30% from Y_d [36]. At the cross section level, the combination of down-quark couplings is different from that from the up-quark cou-
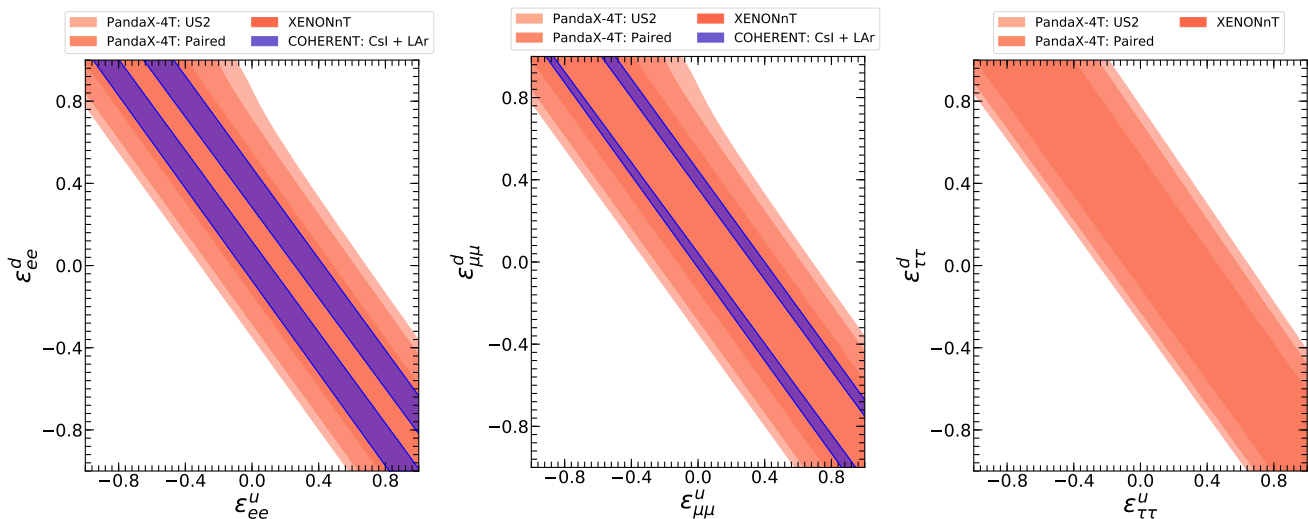
FIG. 4. $\Delta\chi^2$ 90% CL isocontours in the $\varepsilon_{ee}^u - \varepsilon_{ee}^d$ (left graph) and $\varepsilon_{\mu\mu}^u - \varepsilon_{\mu\mu}^d$ (middle graph) and $\varepsilon_{\tau\tau}^u - \varepsilon_{\tau\tau}^d$ (left graph) planes. Results are shown for the PandaX-4T [paired and unpaired ionization-only signals (US2)] as well as for XENONnT data sets. For comparison results from combined analysis of COHERENT CsI+LAr data [43] are shown as well. Results for the combined analysis have a strong overlapp with those from XENONnT so are not displayed. Note that COHERENT measurements are not sensitive to $\varepsilon_{\tau\tau}^q$ NSI parameters.

plings [see Eq. (18)]. However, those differences are small and to a certain degree smooth out at the event rate level.

We have summarized the 1σ level ranges following from these two analyzes in Tab. III in App. A. It is worth comparing these results with those derived recently from a combined analysis of COHERENT data [43]. For diagonal couplings these results are rather comparable to those reported in Ref. [43]. More sizable deviations are found for off-diagonal parameters, in particular for $\varepsilon_{e\mu}^q$ and $\varepsilon_{\mu\tau}^q$ where the COHERENT combined analysis leads to constraints that exceed those found here by about $20\% - 50\%$. Thus, these data sets already provide limits that are comparable with those derived using COHERENT data. Expectations are then that with forthcoming measurements sensitivities to possible new physics in the neutrino sector will improve. Most relevant is the fact that contrary to data coming from stopped-pion sources and/or reactors, measurements from solar neutrino data are sensitive to pure τ flavor parameters.

Finally, results for the two-parameter analysis are shown in Fig. 4. Overlaid are those derived from COHERENT LAr+CsI combined analysis, in the two cases where they apply. The combined analysis is not displayed because the strong overlapp with the XENONnT data result. It is clear that COHERENT data is moderately more sensitive to NSI effects, but results from PandaX-4T+XENONnT already provide complementary information. We understand this behavior as due to smaller statistical uncertainties in the COHERENT data sets, in particular in the last CsI data set release which largely dominates the fit [43].

V. CONCLUSIONS

Recent measurements of nuclear recoils induced by the ^{8}B solar neutrino flux by the PandaX-4T and XENONnT collaborations have opened a new era for both DM searches and neutrino physics. Certainly, for DM searches this implies abandoning the free-background paradigm and adopting new strategies in the quest for DM. For neutrino physics, on the other hand, it provides a new landscape of opportunities that range from precise measurements of the CEvNS cross section (at energies below those employed in stopped-pion neutrino sources) to searches of new physics that can potentially be hidden in the neutrino sector. This would represent a full program, complementary to all the other CEvNS related worldwide efforts.

With a goal of establishing sensitivity to neutrino physics, in this paper we have studied the sensitivity of the PandaX-4T and XENONnT data sets to neutrino NSI. We have presented a full one-parameter analysis as well as a flavor diagonal two-parameter analysis, the latter with mainly the aim of making contact with previous results derived using COHERENT data.

In the one-parameter case, our findings show that with current statistical uncertainties and exposures sensitivities to flavor-diagonal NSI parameters are comparable to those derived using COHERENT data. Sensitivities to flavor off-diagonal parameters are less pronounced, but still competitive with those coming from COHERENT measurements. In the two-parameter case, a comparison with COHERENT recent data analysis demonstrates that with further improvements these experiments have the potential to lead searches for new physics in the neutrino sector through CEvNS measurements. In particular, and in contrast to reactor or stopped-pion sources, because of neutrino flavor mixing these experiments are sensitive to pure τ flavor observables, providing a

Up-type NSI couplings		
Data set	ε_{ee}^u	$\varepsilon_{e\mu}^u$	$\varepsilon_{e\tau}^u$
Paired	$[-0.12, 0.015] \oplus [0.39, 0.52]$	$[-0.28, 0.22]$	$[-0.25, 0.21]$
US2	$[-0.14, 0.0011] \oplus [0.40, 0.54]$	$[-0.30, -0.053] \oplus [0.0062, 0.25]$	$[-0.28, -0.060] \oplus [0.0080, 0.23]$
XENONnT	$[-0.040, 0.080] \oplus [0.32, 0.45]$	$[-0.17, 0.11]$	$[-0.15, 0.11]$
Combined	$[-0.060, 0.010] \oplus [0.39, 0.47]$	$[-0.20, 0.15]$	$[-0.18, 0.14]$
Data set	$\varepsilon_{\mu\mu}^u$	$\varepsilon_{\mu\tau}^u$	$\varepsilon_{\tau\tau}^u$
Paired	$[-0.22, 0.032] \oplus [0.37, 0.62]$	$[-0.50, -0.29] \oplus [-0.030, 0.18]$	$[-0.17, 0.021] \oplus [0.38, 0.57]$
US2	$[-0.25, -0.00053] \oplus [0.40, 0.66]$	$[-0.53, -0.32] \oplus [0.00, 0.21]$	$[-0.20, -0.0021] \oplus [0.40, 0.60]$
XENONnT	$[-0.090, 0.49]$	$[-0.40, 0.070]$	$[-0.060, 0.19] \oplus [0.22, 0.47]$
Combined	$[-0.12, 0.030] \oplus [0.38, 0.53]$	$[-0.42, -0.29] \oplus [-0.020, 0.11]$	$[-0.090, 0.020] \oplus [0.39, 0.50]$
Down-type NSI couplings		
Data set	ε_{ee}^d	$\varepsilon_{e\mu}^d$	$\varepsilon_{e\tau}^d$
Paired	$[-0.11, 0.01] \oplus [0.34, 0.47]$	$[-0.25, 0.20]$	$[-0.22, 0.19]$
US2	$[-0.13, 0.00] \oplus [0.36, 0.49]$	$[-0.27, -0.05] \oplus [0.00, 0.23]$	$[-0.25, -0.040] \oplus [0.010, 0.21]$
XENONnT	$[-0.040, 0.080] \oplus [0.28, 0.40]$	$[-0.15, 0.10]$	$[-0.13, 0.090]$
Combined	$[-0.060, 0.010] \oplus [0.35, 0.42]$	$[-0.18, 0.13]$	$[-0.16, 0.13]$
Data set	$\varepsilon_{\mu\mu}^d$	$\varepsilon_{\mu\tau}^d$	$\varepsilon_{\tau\tau}^d$
Paired	$[-0.20, 0.030] \oplus [0.33, 0.55]$	$[-0.44, -0.28] \oplus [-0.020, 0.14]$	$[-0.15, 0.020] \oplus [0.33, 0.51]$
US2	$[-0.23, 0.00] \oplus [0.36, 0.58]$	$[-0.46, -0.30] \oplus [0.00, 0.17]$	$[-0.18, 0.00] \oplus [0.36, 0.54]$
XENONnT	$[-0.080, 0.43]$	$[-0.35, 0.050]$	$[-0.060, 0.41]$
Combined	$[-0.11, 0.020] \oplus [0.33, 0.47]$	$[-0.37, -0.28] \oplus [-0.010, 0.080]$	$[-0.080, 0.020] \oplus [0.34, 0.45]$

TABLE III. 1σ CL intervals for ε_{ij}^u (upper table) and ε_{ij}^d (lower table) derived from PandaX-4T (paired and US2) and XENONnT data sets as well as from a combined analysis of all data. As a function of the NSI parameters, event rates tend to be symmetric around a value close to zero. The non-overlapping intervals in all cases are a result of this behavior.

new channel for this flavor that is difficult to isolate in current solar neutrino data [52].

Future data sets with improved exposures and statistical uncertainties will improve upon the constraints we presented. For example, increasing the exposure by a factor of 5, we checked that sensitivities to ε_{ee}^u interactions may improve by about 50%. Given that we are just now working with initial results from Xenon-based DM experiments, it is likely that combined with electron recoil measurements, data from CEvNS induced by the ^{8}B solar neutrino flux might lead searches for new physics using this type of technology and perhaps pave the way for unexpected discoveries.

couplings but $\varepsilon_{\tau\tau}^q$, these results should be contrasted with those derived using COHERENT CsI+LAr data and/or Ge data [43, 44]. This is the first time that constraints for $\varepsilon_{\tau\tau}^q$ have been derived from pure solar neutrino CEvNS related data sets.

Appendix A: Summary of NSI parameters limits

In this appendix we collect the 1σ ranges for up- and down-quark NSI parameters. Results are shown in Tab. III. For all

ACKNOWLEDGMENTS

[1] Z. Bo et al. (PandaX) (2024), 2407.10892.

[2] E. Aprile et al. (2024), 2408.02877.

[3] D. Akimov et al. (COHERENT), Science **357**, 1123 (2017), 1708.01294.

[4] D. Akimov et al. (COHERENT), Phys. Rev. D **100**, 115020 (2019), 1909.05913.

[5] S. Adamski et al. (2024), 2406.13806.

[6] J. Monroe and P. Fisher, Phys. Rev. D **76**, 033007 (2007), 0706.3019.

[7] J. D. Vergados and H. Ejiri, Nucl. Phys. B **804**, 144 (2008), 0805.2583.

[8] L. E. Strigari, New J. Phys. **11**, 105011 (2009), 0903.3630.

[9] J. Billard, L. Strigari, and E. Figueroa-Feliciano, Phys. Rev. D **89**, 023524 (2014), 1307.5458.

[10] C. A. J. O'Hare, Phys. Rev. Lett. **127**, 251802 (2021), 2109.03116.

[11] B. Aharmim et al. (SNO), Phys. Rev. C **88**, 025501 (2013), 1109.0763.

[12] J. Aalbers et al., J. Phys. G **50**, 013001 (2023), 2203.02309.

[13] D. G. Cerdeno, J. H. Davis, M. Fairbairn, and A. C. Vincent, JCAP **04**, 037 (2018), 1712.06522.

[14] B. Dutta, S. Liao, L. E. Strigari, and J. W. Walker, Phys. Lett. B **773**, 242 (2017), 1705.00661.

[15] D. Aristizabal Sierra, N. Rojas, and M. H. G. Tytgat, JHEP **03**, 197 (2018), 1712.09667.

[16] D. Aristizabal Sierra, B. Dutta, S. Liao, and L. E. Strigari, JHEP **12**, 124 (2019), 1910.12437.

[17] B. Dutta and L. E. Strigari, Ann. Rev. Nucl. Part. Sci. **69**, 137 (2019), 1901.08876.

[18] J. Billard, L. E. Strigari, and E. Figueroa-Feliciano, Phys. Rev. D **91**, 095023 (2015), 1409.0050.

[19] D. Alonso-González, D. W. P. Amaral, A. Bariego-Quintana, D. Cerdeño, and M. de los Rios, JHEP **12**, 096 (2023), 2307.05176.

[20] D. Aristizabal Sierra, R. Branada, O. G. Miranda, and G. Sanchez Garcia, JHEP **12**, 178 (2020), 2008.05080.

[21] D. Aristizabal Sierra, O. G. Miranda, D. K. Papoulias, and G. S. Garcia, Phys. Rev. D **105**, 035027 (2022), 2112.12817.

[22] M. Cadeddu, N. Cargioli, F. Dordei, C. Giunti, Y. F. Li, E. Picciau, and Y. Y. Zhang, JHEP **01**, 116 (2021), 2008.05022.

[23] C. Giunti and C. A. Ternes, Phys. Rev. D **108**, 095044 (2023), 2309.17380.

[24] D. Aristizabal Sierra, V. De Romeri, L. J. Flores, and D. K. Papoulias, Phys. Lett. B **809**, 135681 (2020), 2006.12457.

[25] J. B. Dent, B. Dutta, J. L. Newstead, and L. E. Strigari, Phys. Rev. D **95**, 051701 (2017), 1607.01468.

[26] D. Aristizabal Sierra, V. De Romeri, L. J. Flores, and D. K. Papoulias, JCAP **01**, 055 (2022), 2109.03247.

[27] D. Z. Freedman, Phys. Rev. D **9**, 1389 (1974).

[28] L. M. Sehgal, Phys. Lett. B **162**, 370 (1985).

[29] O. Tomalak, P. Machado, V. Pandey, and R. Plestid, JHEP **02**, 097 (2021), 2011.05960.

[30] N. Mishra and L. E. Strigari, Phys. Rev. D **108**, 063023 (2023), 2305.17827.

[31] K. S. Kumar, S. Mantry, W. J. Marciano, and P. A. Souder, Ann. Rev. Nucl. Part. Sci. **63**, 237 (2013), 1302.6263.

[32] D. Aristizabal Sierra, J. Liao, and D. Marfatia, JHEP **06**, 141 (2019), 1902.07398.

[33] D. Aristizabal Sierra, Phys. Lett. B **845**, 138140 (2023), 2301.13249.

[34] R. H. Helm, Phys. Rev. **104**, 1466 (1956).

[35] D. Baxter et al., Eur. Phys. J. C **81**, 907 (2021), 2105.00599.

[36] N. Vinyoles, A. M. Serenelli, F. L. Villante, S. Basu, J. Bergström, M. C. Gonzalez-Garcia, M. Maltoni, C. Peña Garay, and N. Song, Astrophys. J. **835**, 202 (2017), 1611.09867.

[37] J. Barranco, O. G. Miranda, and T. I. Rashba, JHEP **12**, 021 (2005), hep-ph/0508299.

[38] Y. Farzan and M. Tortola, Front. in Phys. **6**, 10 (2018), 1710.09360.

[39] M. C. Gonzalez-Garcia, M. Maltoni, and J. Salvado, JHEP **05**, 075 (2011), 1103.4365.

[40] M. C. Gonzalez-Garcia and M. Maltoni, JHEP **09**, 152 (2013), 1307.3092.

[41] I. Esteban, M. C. Gonzalez-Garcia, M. Maltoni, I. Martinez-Soler, and J. Salvado, JHEP **08**, 180 (2018), [Addendum: JHEP 12, 152 (2020)], 1805.04530.

[42] P. Coloma, M. C. Gonzalez-Garcia, M. Maltoni, J. a. P. Pinheiro, and S. Urrea, JHEP **08**, 032 (2023), 2305.07698.

[43] V. De Romeri, O. G. Miranda, D. K. Papoulias, G. Sanchez Garcia, M. Tórtola, and J. W. F. Valle, JHEP **04**, 035 (2023), 2211.11905.

[44] J. Liao, D. Marfatia, and J. Zhang (2024), 2408.06255.

[45] A. Friedland, M. L. Graesser, I. M. Shoemaker, and L. Vecchi, Phys. Lett. B **714**, 267 (2012), 1111.5331.

[46] D. Buarque Franzosi, M. T. Frandsen, and I. M. Shoemaker, Phys. Rev. D **93**, 095001 (2016), 1507.07574.

[47] P. F. de Salas, S. Gariazzo, P. Martínez-Miravé, S. Pastor, and M. Tórtola, Phys. Lett. B **820**, 136508 (2021), 2105.08168.

[48] A. Esteban-Pretel, R. Tomas, and J. W. F. Valle, Phys. Rev. D **76**, 053001 (2007), 0704.0032.

[49] S. Jana and Y. Porto (2024), 2407.06251.

[50] P. F. de Salas, D. V. Forero, S. Gariazzo, P. Martínez-Miravé, O. Mena, C. A. Ternes, M. Tórtola, and J. W. F. Valle, JHEP **02**, 071 (2021), 2006.11237.

[51] S. J. Parke, Phys. Rev. Lett. **57**, 1275 (1986), 2212.06978.

[52] K. J. Kelly, N. Mishra, M. Rai, and L. E. Strigari (2024), 2407.03174.